

Solar image deconvolution by generative adversarial network

Long Xu¹, Wen-Qing Sun¹, Yi-Hua Yan¹ and Wei-Qiang Zhang²

¹ Key Laboratory of Solar Activity, National Astronomical Observatories, Chinese Academy of Sciences, Beijing 100101, China; lxu@nao.cas.cn

² College of Mathematics and Statistics, Shenzhen University, Shenzhen 518060, China

Received 2020 February 23; accepted 2020 April 30

Abstract With aperture synthesis (AS) technique, a number of small antennas can be assembled to form a large telescope whose spatial resolution is determined by the distance of two farthest antennas instead of the diameter of a single-dish antenna. In contrast from a direct imaging system, an AS telescope captures the Fourier coefficients of a spatial object, and then implement inverse Fourier transform to reconstruct the spatial image. Due to the limited number of antennas, the Fourier coefficients are extremely sparse in practice, resulting in a very blurry image. To remove/reduce blur, “CLEAN” deconvolution has been widely used in the literature. However, it was initially designed for a point source. For an extended source, like the Sun, its efficiency is unsatisfactory. In this study, a deep neural network, referring to Generative Adversarial Network (GAN), is proposed for solar image deconvolution. The experimental results demonstrate that the proposed model is markedly better than traditional CLEAN on solar images. The main purpose of this work is visual inspection instead of quantitative scientific computation. We believe that this will also help scientists to better understand solar phenomena with high quality images.

Key words: deep learning (DL) — generative adversarial network (GAN) — solar radio astronomy — image reconstruction — aperture synthesis

1 INTRODUCTION

The spatial resolution of a single-dish antenna is limited by the diameter of the dish, subject to λ/D , where λ represents wavelength and D is the dish diameter. It is a considerable challenge to construct a large single-dish antenna, considering building materials, building technology, architecture and cost. Aperture synthesis (AS) synthesizes a bunch of small antennas to form a big antenna whose spatial resolution is determined by the distance of two farthest antennas, namely maximum baseline, still subject to λ/D , where D is the maximum baseline. Nowadays, AS has been developed intensively in radio astronomy. Many large radio telescopes, like world-wide low frequency array (LOFAR), Atacama large millimeter array (ALMA) and square meter array (SKA), domestic MingantU SpEctral Radioheliograph (MUSER) have been constructed. MUSER is a solar dedicated AS telescope with the maximum baseline of 3 km, consisting of 100 small antennas. Each pair of antennas compose of an interferometer, recording a Fourier component at each time. We can have $n \times (n - 1)/2$ interferometers given n antennas, thus $n \times (n - 1)/2$ Fourier components

can be obtained. Taking advantage of the earth rotation, one can get more Fourier components. Nevertheless, the Fourier components are very sparse in practice due to the limited number of antennas, resulting in blurry image. For an AS telescope, image quality degradation is caused by sparse Fourier sampling in frequency domain. Fourier sampling is described to a frequency-domain image multiplied by a sampling function as shown in Figure 1(a). It is corresponding to a spatial image convolved by a point spread function (PSF) or dirty beam as shown in Figure 1(b). The sampling function and the PSF are the Fourier transform pairs. Convolution with the PSF/dirty beam would result in a dirty image which looks blurry. This happens because the PSF has strong sidelobes which would cause signal aliasing. To eliminate aliasing, deconvolution, which is the inverse process of convolution, was employed. In radio astronomy, a category of deconvolution algorithms, namely CLEAN (Högbom 1974; Wakker & Schwarz 1988; Cornwell 2008), has been extensively studied.

Deconvolution is a deblurring problem essentially. There are basically four categories of image deblurring methods in the literature. The first, CLEAN

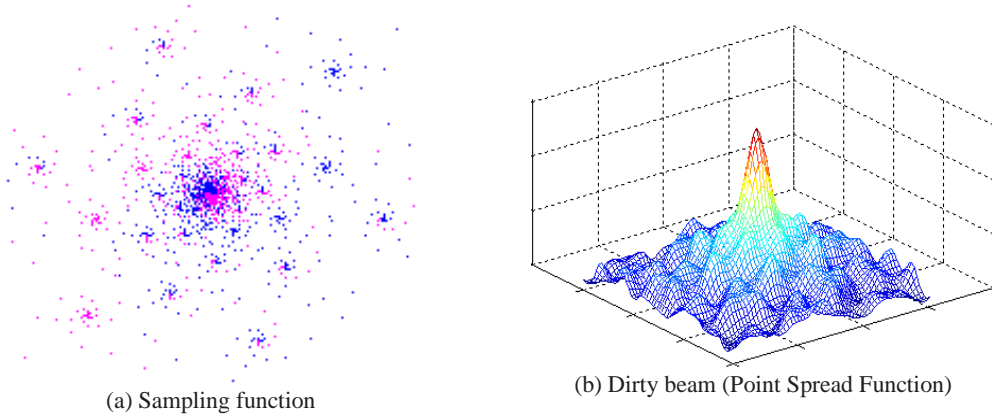


Fig. 1 Sampling function of an aperture synthesis.

(Högbom 1974; Wakker & Schwarz 1988; Cornwell 2008), is mostly used in deconvolution of point source. The second solves an inverse problem by imposing regularized constraint, such as Total Variation (TV) (Ma et al. 2008; Wen et al. 2011; Rudin et al. 1992; Beck & Teboulle 2009), sparseness (Elad & Aharon 2006; Zhang et al. 2014; Wenger et al. 2010; Xu et al. 2018a). The third is developed on multi-scale signal decomposition (Wakker & Schwarz 1988; Cornwell 2008), such as wavelet, exploiting the multi-scale feature and spectral representation of signal. The last is a learning based method (Xiang et al. 2015; Su & Basu 2002; Rubinstein et al. 2012, 2009; Xu et al. 2014), which learns signal representation by using machine learning.

The reconstructed image from an AS system usually looks very blurry since highly sparse sampling in Fourier domain. This situation is very common in radio astronomy observation. To address this problem, CLEAN algorithm was widely used. This paper introduces a novel deconvolution algorithm based on Generative Adversarial Network (GAN) (Goodfellow et al. 2014), to accomplish image deconvolution. It should be pointed out that deep learning models are mostly used in image processing. As they are applied to scientific data, their outputs cannot easily return to original data range, which makes computing of physical parameters invalid. Thus, this proposed model is mainly with the purpose of visual inspection instead of quantitative analysis, through reconstructing high-quality images from dirty images. We believe that this is also important for scientific research, so that the scientists can better find/understand interesting solar activities from current observations.

The rest of this paper is organized as follows. Section 2 gives the principle of AS. Section 3 gives the details of the proposed deep neural network for image deconvolution. Experimental results are provided in Section 4. The final section draws our conclusions.

2 APERTURE SYNTHESIS PRINCIPLE

Given original spatial image by $I(x, y)$, the corresponding image in frequency domain by $V(u, v)$, they are the Fourier transform pairs, named by brightness function and visibility function, respectively. If there are all Fourier coefficients, $I(l, m)$ can be completely reconstructed. However, the real situation is that $V(u, v)$ is sparsely sampled in Fourier domain. So, a sampled visibility function $V^D(u, v)$ is only available in an AS system, which is represented by

$$V^D(u, v) = V(u, v) \times S(u, v), \quad (1)$$

where $S(u, v)$ is the sampling function in frequency domain. Applying inverse Fourier transform to both sides of Equation (1), we can get

$$I^D(l, m) = \iint_{\Sigma} V(u, v) S(u, v) \exp(-i2\pi(ul+vm)) dudv, \quad (2)$$

where $I^D(l, m)$ is a dirty image deduced from the Fourier transform of $V^D(u, v)$. Since convolution operation in frequency domain is equivalent to multiplication in spatial domain, Equation (2) can be rewritten into

$$I^D(l, m) = I(l, m) \otimes B^D(l, m), \quad (3)$$

where the symbol “ \otimes ” denotes convolution operator, and

$$B^D(l, m) = \iint_{\Sigma} S(u, v) \exp(-i2\pi(ul+vm)) dudv, \quad (4)$$

which is the dirty beam or PSF. For easy understanding, we draw a sketch map in Figure 2 for illustrating the imaging process of an AS system, from both frequency and spatial domain.

From Equation (3), it is only possible to derive $I^D(x, y)$ instead of $I(x, y)$, i.e., dirty image in spatial domain, while the ideal image $I(x, y)$ is unavailable

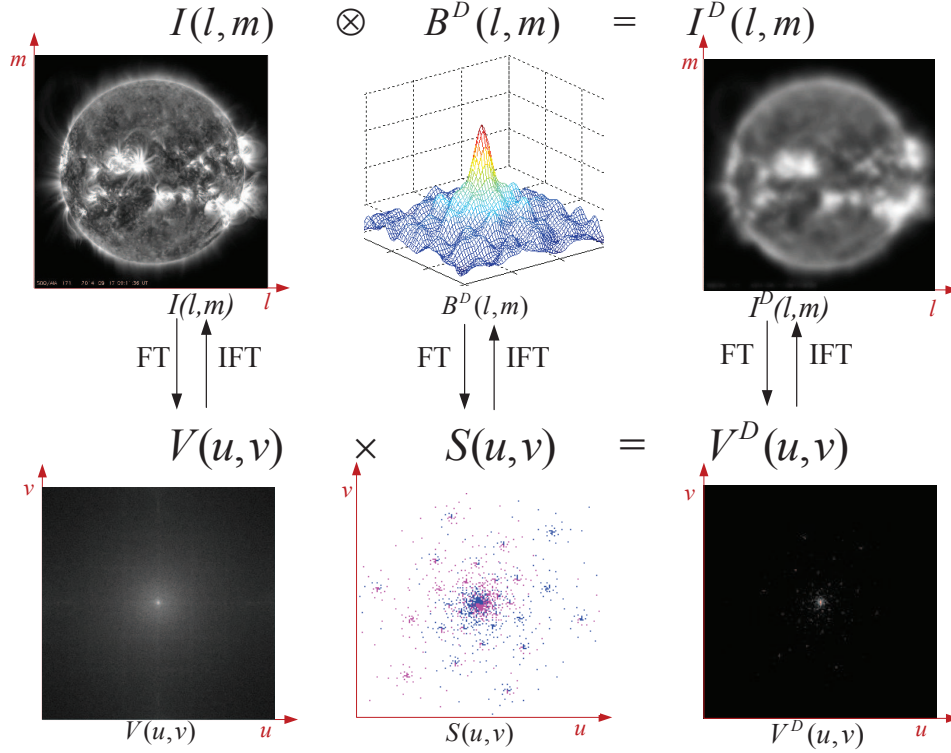


Fig. 2 Imaging principle of aperture synthesis.

since it is polluted by dirty beam $B(x, y)$. To restore $I(x, y)$, we have to delete dirty beam $B(x, y)$ from the left side of Equation (3). This process is usually named “CLEAN” deconvolution. For point source, like stellar object, Högbom, et. al. proposed a classical Högbom CLEAN algorithm, which was witnessed to perform well given dirty beam. However, it was unsatisfactory for an extended source, like the Sun, so a bunch of algorithms were proposed later, such as multi-resolution CLEAN (MRC), multi-scale Clean and wavelet CLEAN.

3 NETWORK FOR IMAGE DECONVOLUTION

Recently, deep learning (DL) (Goodfellow et al. 2014; Xu et al. 2018b; Hinton & Salakhutdinov 2006; Hinton et al. 2006; Bengio 2009; LeCun et al. 1989, 1998) was intensively developed and achieved big success in many application fields, such as image processing, speech recognition, natural language understanding, pattern recognition and computer vision. The advantages of DL lie in twofold. First, it can learn a model from mass of data, which would be more applicable in practice. While traditional machine learning model or physical model would not make full use of mass of available data. Second, DL does not need to fully acquire knowledges of a physical process. It would not establish a mathematical

model at all. Instead, an extreme non-learning relation between input and output is learnt in a data-intensive manner. This advantage of DL makes itself possess more flexibility and applicability. GAN (Goodfellow et al. 2014; Xu et al. 2018b) is a DL model which was recently raised and has been extensively investigated in many kinds of applications, especially image reconstruction, such as image denoising, image synthesis, super-resolution. A GAN is comprised of a generator and a discriminator. The generator makes fake image close to real one/ground-truth, while the discriminator distinguishes between fake image and real one. Repeating adversarial learning between them, a powerful generator can be learnt, which could generate image very close to real one. The principle of GAN is originated from zero-sum minimax game, which is mathematically represented by

$$G^* = \arg \min_G \max_D \mathcal{L}_{\text{GAN}}(G, D),$$

$$\mathcal{L}_{\text{GAN}}(G, D) = \mathbb{E}_y [\log D(y)] + \mathbb{E}_{x, z} [\log(1 - D(G(x, z)))],$$
(5)

where D represents a detector, G represents a generator, y is a real image and $G(x, z)$ is a fake image. In Equation (5), y is coming from a distribution of real data, x is coming from our simulated data (e.g., degraded images in image processing), and z is coming from a random noise. For

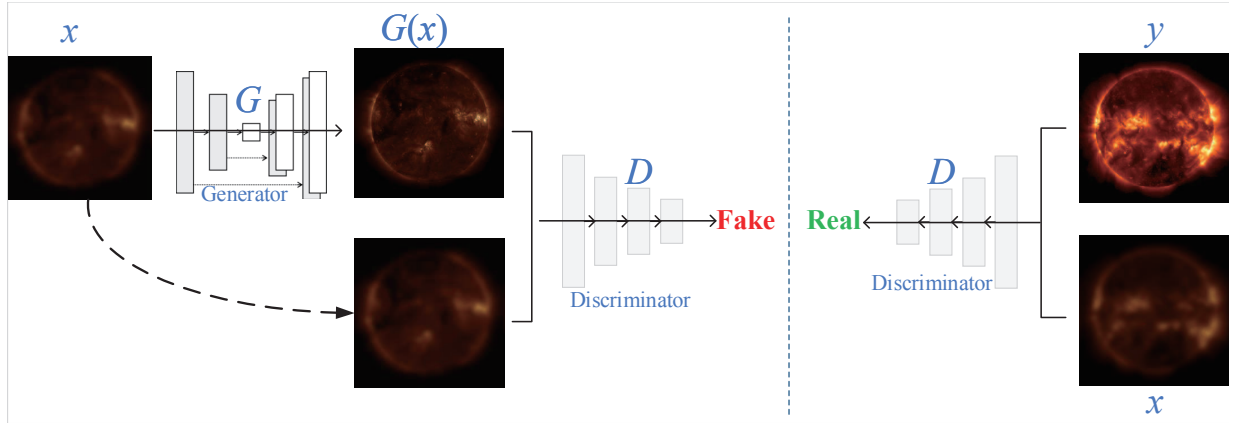


Fig. 3 Principle diagram of image deconvolution network.

optimizing D , we expect the larger $D(y)$ on the real data and the smaller $D(G(x, z))$ on the fake data generated by the generator G . While for optimizing G , we expect that it can generate enough realistic sample $G(x, z)$ to cheat D successfully. During training process, D and G are optimized alternatively, by fixing one and optimizing the other.

As Equation (5) indicated, a general GAN only discriminate fake and true of the output. However, most of image processing tasks, e.g., well-known image-to-image translation (Isola et al. 2016), require the correspondences between inputs and outputs besides discriminating fake and true. For this purpose, the conditional GAN (cGAN) was proposed, which is described by

$$G^* = \arg \min_G \max_D \mathcal{L}_{\text{cGAN}}(G, D),$$

$$\mathcal{L}_{\text{cGAN}}(G, D) = \mathbb{E}_{x,y}[\log D(x, y)] + \mathbb{E}_{x,z}[\log(1 - D(x, G(x, z)))], \quad (6)$$

where $D(x, y)$, $D(x, G(x, z))$ indicates that D needs not only distinguish the real and the fake, but also tell the correspondence between them. In Isola et al. (2016), Phillip Isola et.al. described a cGAN model for image-to-image translation, namely pix2pix. In this work, the network for image deconvolution is on the basis of pix2pix as demonstrated in Figure 3, while the optimization objective is revised for facilitating our specific task. Besides cGAN loss and L1 loss of spatial domain ($\mathcal{L}_{L1}^I(G) = \mathbb{E}_{x,y,z}[\|y - G(x, z)\|_1]$) in pix2pix network Isola et al. (2016), a new loss, namely perceptual loss (Johnson et al. 2016), is also introduced additionally as,

$$\mathcal{L}_{L1}^P(G) = \mathbb{E}_{x,y,z}[\|\Phi(y) - \Phi(G(x, z))\|_1], \quad (7)$$

where $\Phi(\cdot)$ represents the feature of an image, specifically, VGG feature from a pre-trained VGG-16 model (Simonyan & Zisserman 2014). Here, the feature maps of

the first four layers of a VGG-16 network are extract to give $\Phi(y)$ and $\Phi(G(x, z))$. Thus, the final objective is

$$G^* = \arg \min_G \max_D \mathcal{L}_{\text{cGAN}}(G, D) + \lambda_1 \mathcal{L}_{L1}^I(G) + \lambda_2 \mathcal{L}_{L1}^P(G). \quad (8)$$

In our model, the generator is a classical UNet, consisting of multiple layers of convolution and transposed convolution as illustrated in Figure 4. From Figure 4, UNet is in the shape of an auto-encoder. The encoder gets compressed representation of the input, while the decoder decompresses this representation to reconstruct the input. The most noteworthy feature of UNet is the skip connection between corresponding layers of the encoder and the decoder. This skip connection can combine both high level semantic information and low level features of an image, benefiting image processing tasks, especially for images with less semantic information, such as medical and astronomy images. The discriminator is a general convolution neural network consisting of five convolution layers.

Image generation/reconstruction, such as image deblurring, denoising and super-resolution, has been well investigated in the literature (Kupyn et al. 2017; KupynOrest 2019; Nah et al. 2016; Yan & Wang 2017). Image deconvolution is a typical image generation problem. Usually, in radio astronomy, it was handled by ‘‘CLEAN’’ algorithm (Högbom 1974; Wakker & Schwarz 1988; Cornwell 2008). Two conditions should be held for the success of the CLEAN algorithm on image deconvolution. One is that the signal should be point source, the other is that dirty beam should be exactly known, which means the dirty beam of actual system and the ideal one are exactly the same. However, in practice, these two conditions do not hold so that the efficiency of the CLEAN algorithm is compromised. The proposed model is learnt from data without any constraint, which is completely data-driven, so it has more competitive advantages in the era of big data.

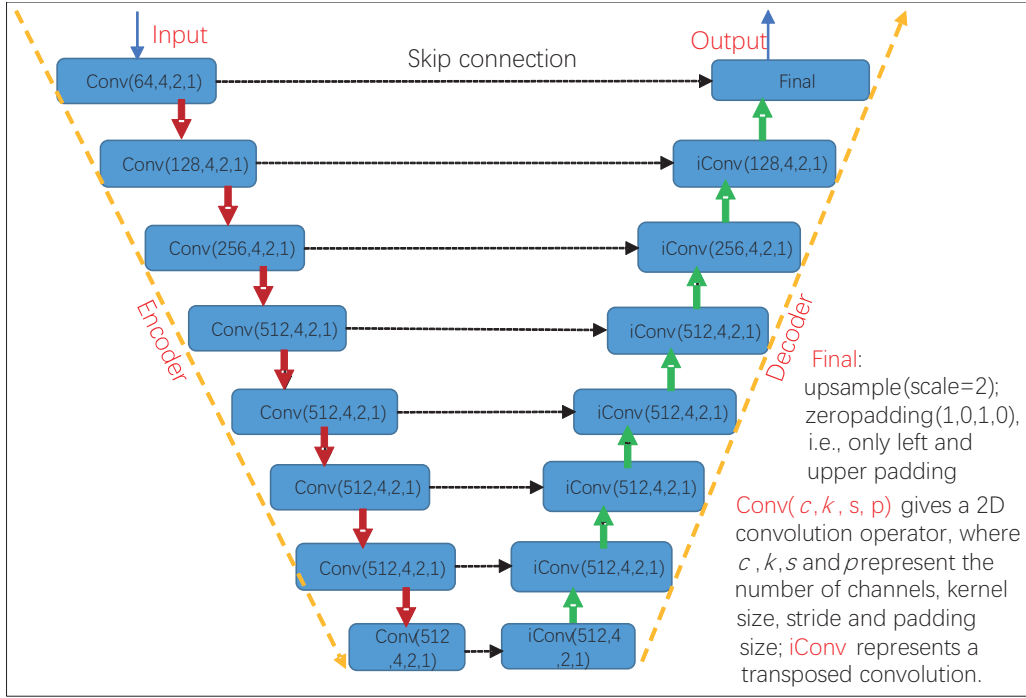


Fig. 4 The proposed model for AS image deconvolution.

4 EXPERIMENTAL RESULTS

To evaluate the proposed model, a database consisting original/clear and dirty image pairs is firstly established. We collected 41 096 images of 193 Å from Atmospheric Imaging Assembly (AIA) of Solar Dynamics Observatory (SDO) as ground-truth/clear images. Then, we apply MUSER-I dirty beam (as shown in Fig. 1(b)) to these clear images, resulting in corresponding dirty images. For training, validation and testing, the database is split into three parts: 8000 image pairs for validation, 8000 image pairs for testing and the remaining for training. The full implementation (based on Pytorch) and the trained network can be accessed via <https://github.com/filterbank/solarGAN>. From the statistics of experimental results, we can observe and conclude that:

- (1) In the beginning, the generated image is with low quality since the training process is far from convergence;
- (2) After about 5000 loops, the learnt model can be stable, generating high quality images as shown in Figure 6, where the left column gives dirty images, the middle column shows output images after GAN deconvolution, the right column shows original images;
- (3) The learnt model can restore image details/structures well, as shown in Figure 6(b). Compared with dirty image in Figure 6(a), the reconstructed one contains more details of an image;

Table 1 Performance Verification of the Proposed Network with Different Loss Function

Loss function	PSNR	SSIM
$\mathcal{L}_{cGAN(G,D)} + \mathcal{L}_{L1}^I$	38.0575	0.9561
$\mathcal{L}_{cGAN(G,D)} + \mathcal{L}_{L1}^I + \mathcal{L}_{L1}^P$	38.4442	0.9609
$\mathcal{L}_{cGAN(G,D)} + \mathcal{L}_{L2}^I$	35.2378	0.9316
$\mathcal{L}_{cGAN(G,D)} + \mathcal{L}_{L2}^I + \mathcal{L}_{L2}^P$	37.3543	0.94727

- (4) We also verify the effectiveness of spatial loss and perceptual loss as claimed in Equation (7) for our task. The PSNR and SSIM on the whole testing dataset are compared in Table 1. It can be observed that the best result is coming from the combination of cGAN loss, spatial-domain L1 loss and perceptual L1 loss.

For objective measurement of image quality, peak signal to noise ratio (PSNR), visual signal to noise ratio (VSNR) (Chandler & Hemami 2007), structural similarity index measurement (SSIM) (Wang et al. 2004), Feature Similarity (FSIM) (Zhang et al. 2011) and a metric designed for solar image named perception evaluation (PE) (Deng et al. 2015) are employed for evaluating the proposed model. PSNR measures the absolute difference of pixel-to-pixel of two images. VSNR measures visual fidelity of natural image from aspects of near-threshold and suprathreshold properties of human vision. SSIM may ignore the pixel-to-pixel difference, while pays more attention to the similarity of image structure. FSIM has the same principle of SSIM for measuring structural similarity, additionally considering phase congruency. PE

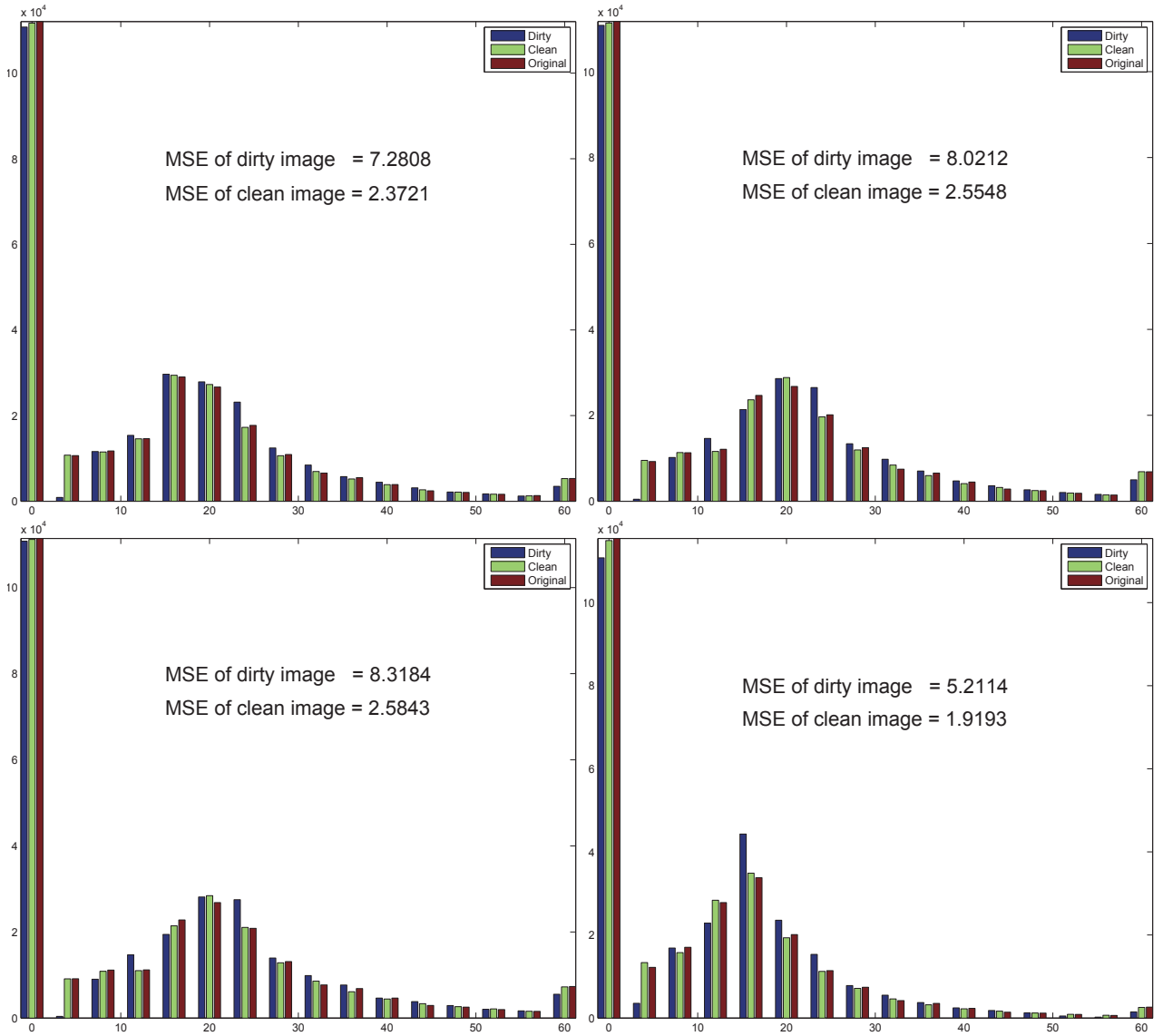


Fig. 5 Histograms of dirty image, clean/deconvolved image and original image (For more clearly, only 16 bins with the same interval from 0 to 64 are shown in histogram. We discard the pixels with pixel value larger than 64 in histogram statistics since they account for very small percent).

was specifically designed for solar image by considering multi-fractal property of texture features. The statistics of PSNR, SSIM, FSIM and VSNR are gathered in Table 2 for evaluating our proposed model. From Table 2, average 5.31dB PSNR, 7.27% SSIM, 13% FSIM and 4.15% VSNR gains can be achieved by the proposed model. In addition, we found that SSIM works well for measuring blurriness of image, however, user designed parameters have a significant impact on SSIM indexes. Here, we use the default configuration in Wang et al. (2004). It can be observed that PE is a very good image quality indicator for measuring solar image quality. From Table 2, more than 50% PE improvement is achieved by the proposed deconvolution algorithm.

In a real situation, a small disturbance exists, which will make the situation more complicated, so the model should be more flexible and robust for addressing these complicated situations. For this purpose, we introduce one of the noises, namely, Gaussian white noise, in our simulation for checking the flexibility and robustness of the proposed model. The experiment results, as listed in the lower part of Table 2, indicate that the proposed model still performs well in the case of small disturbance. From Table 2, the SSIM improvement is remarkable, up to 23.4%. The reason lies in that the proposed model can accomplish not only deconvolution but also denoising, so that it achieves more for this case than the case without noise. In fact, deep learning has been proved to be highly efficient in image denoising (Tian et al. 2019). Thus, we

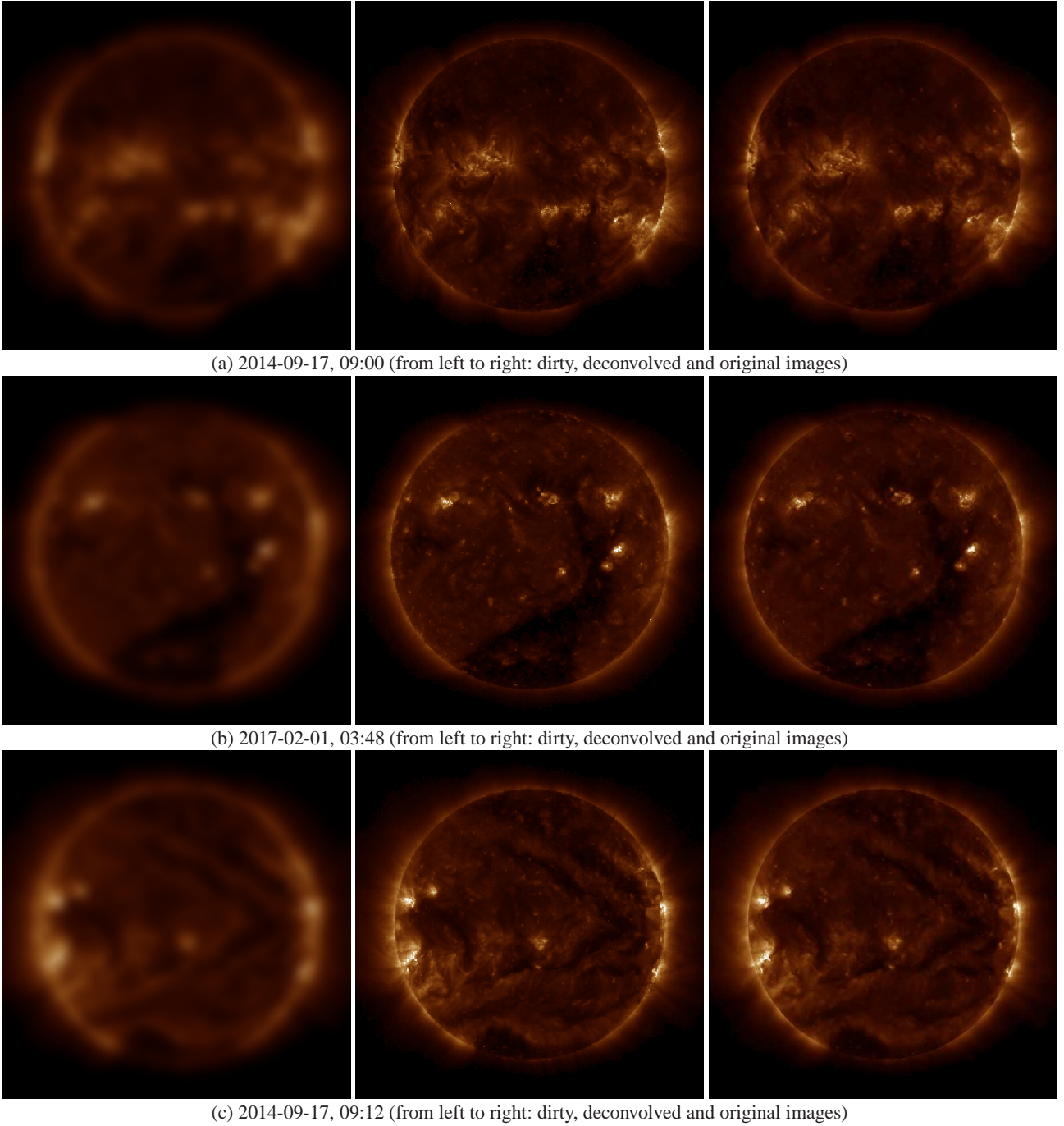


Fig. 6 Image quality comparison between dirty images (*left*), deconvolved images (*middle*) and original one (*right*) (SDO/AIA, 193 Å, dirty images are derived from MUSER-I sampling).

conclude that the proposed model is robust for handling small noise, partially because it is a data driven model.

We also compare the histograms of a dirty image, a deconvolved image and an original image in Figure 5. It can be found that the deconvolved image looks more like the original one regarding histogram. In addition, we use mean square error (MSE) to measure the distance between two histograms of deconvolved image and dirty image relative to that of original image, respectively. The

statistics of MSEs (given in text over the histograms) show that the MSE of deconvolved image is much less than that of dirty image, which well accords with the statistics in Table 2.

For comparison between the proposed model and traditional Högbom CLEAN, the dirty image in Figure 6(a) is processed by Högbom CLEAN. The results of Högbom CLEAN are shown in Figure 7, where Figures 7(a) and (b) demonstrate the images of bright points after

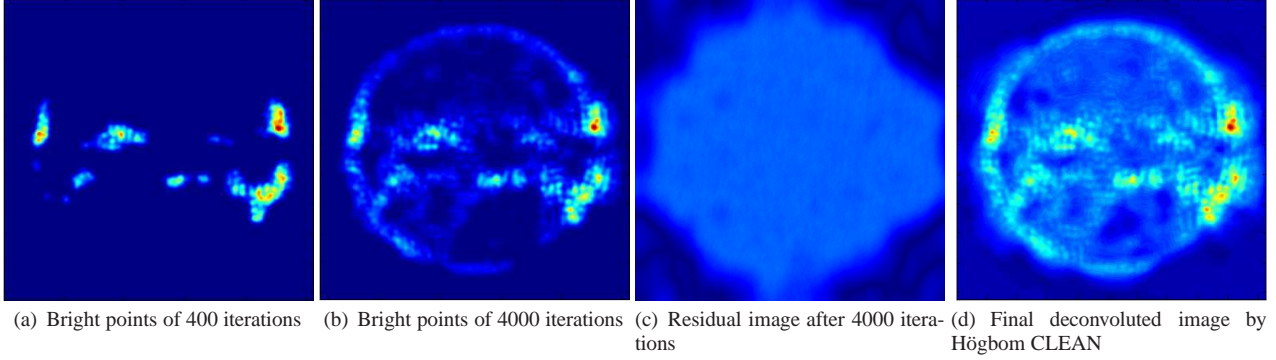


Fig. 7 The reconstructed image by using Högbom CLEAN ((a) and (b) only shows bright points without quiet solar background; here only grayscale images are processed since Högbom CLEAN is implemented on grayscale image).

Table 2 Performance Comparisons

Test image	PSNR (dB)		SSIM		FSIM		VSNR		PE	
	Clean	Dirty	Clean	Dirty	Clean	Dirty	Clean	Dirty	Clean	Dirty
t_1	43.8750	38.3328	0.9774	0.9057	0.9814	0.8658	33.8485	31.6998	0.8538	0.4743
t_2	44.2428	38.5245	0.9779	0.9094	0.9821	0.8687	34.6958	31.5655	0.8435	0.4871
t_3	44.2086	38.3940	0.9777	0.9066	0.9816	0.8662	34.2766	31.6877	0.8503	0.4909
t_4	43.5998	37.7312	0.9780	0.8964	0.9823	0.8608	32.7893	31.1593	0.8387	0.5109
t_5	43.7245	38.6883	0.9781	0.9112	0.9843	0.8699	34.5025	31.5727	0.8344	0.5452
t_6	43.6156	38.6416	0.9780	0.9104	0.9842	0.8686	34.7588	31.6789	0.8434	0.5499
t_7	43.6732	38.6577	0.9763	0.9104	0.9832	0.8647	33.2941	32.3627	0.8443	0.5855
t_8	43.6642	38.5419	0.9760	0.9082	0.9831	0.8634	32.9892	32.4592	0.8546	0.5864
t_9	44.4864	39.5934	0.9788	0.9246	0.9830	0.8813	31.5974	32.9839	0.8677	0.6495
t_{10}	45.2665	40.1188	0.9795	0.9321	0.9836	0.8886	30.6602	32.9599	0.8663	0.6551
Average	44.0357	38.7224	0.9738	0.9115	0.9829	0.8698	33.3412	30.7158	0.8497	0.5535
Gain	5.3133		0.0743(7.27%)		0.1131(13.00%)		1.3282(4.15%)		0.2962(53.52%)	
t_1	41.9677	38.4872	0.9727	0.7910	0.9775	0.8634	33.3985	31.2786	0.8560	0.4732
t_2	42.1381	38.6822	0.9729	0.7911	0.9783	0.8666	34.0933	31.3234	0.8570	0.4830
t_3	42.0155	38.5471	0.9724	0.7911	0.9774	0.8644	33.8954	31.3592	0.8646	0.4895
t_4	41.7254	37.8749	0.9730	0.7897	0.9784	0.8589	34.1138	30.9221	0.8569	0.5099
t_5	41.8152	38.8721	0.9728	0.7847	0.9789	0.8666	33.1041	31.1079	0.8790	0.6447
t_6	41.5429	38.8339	0.9731	0.7846	0.9792	0.8660	33.5437	31.2165	0.8488	0.5392
t_7	40.9006	38.8615	0.9718	0.7876	0.9790	0.8638	30.3722	31.7513	0.8601	0.5816
t_8	40.6091	38.7367	0.9712	0.7870	0.9789	0.8621	30.8858	31.8612	0.8614	0.5769
t_9	42.0649	39.7943	0.9749	0.7903	0.9794	0.8795	32.7078	32.3192	0.8829	0.6394
t_{10}	43.1939	40.3570	0.9761	0.7884	0.9796	0.8867	31.9447	32.0454	0.8418	0.5351
Average	41.7973	38.9047	0.9731	0.7886	0.9787	0.8678	32.8059	31.5185	0.8608	0.5472
Gain	2.8926		0.1845(23.40%)		0.1109(12.78%)		1.2874(4.08%)		0.3136(57.31%)	

Test images are indexed by $t_i, i = 1, 2, \dots, 10$, representing ‘2012–08–31 19:48:06UT’, ‘2014–09–17 08:48:06UT’, ‘2014–09–17 09:00:06UT’, ‘2014–09–17 09:12:06UT’, ‘2015–05–28 12:48:06UT’, ‘2016–05–18 02:00:05UT’, ‘2016–05–18 02:12:05UT’, ‘2017–02–01 03:48:04UT’, ‘2017–02–01 04:00:04UT’, ‘2017–09–03 00:48:04UT’ from top to down.

Högbom CLEAN of 400 and 4000 iterations, respectively. Figure 7(c) is the residual image corresponding to Figure 7(b). Figure 7(d) gives the final deconvoluted image which combines the residual image (Fig. 7(c)) and the image of bright points (Fig. 7(b)). From Figure 7, it can be concluded that Högbom CLEAN can successfully restore bright points in an image, however fail to restore image details. This conclusion also confirms that Högbom CLEAN is designed for point source instead of extended source. Comparing Figure 7 and Figure 6, the proposed model is dramatically superior to Högbom CLEAN on restoring image details/fine structures.

5 CONCLUSIONS

This paper makes an effort on a deep learning model for solar image deconvolution. By adversarial learning on the pairs of original image and dirty image in a GAN framework, a powerful generator is learnt for deconvolving dirty image. The experimental results demonstrate that the proposed model can recover the details of solar image much better than the traditional CLEAN. In addition, the proposed model is data-driven instead of physical model. For this reason, it is more applicable under some complex situations, even unknown the PSF. It should be pointed that the proposed model is mostly concerned with visual

inspection instead of rigorous scientific analysis currently. In our near-future work, we will place more effort on the scientific research of our model.

Acknowledgements This work was partially supported by the National Natural Science Foundation of China (NSFC)(Grant Nos. 61572461, 61811530282, 61872429, 11790301 and 11790305).

References

- Beck, A., & Teboulle, M. 2009, IEEE Transactions on Image Processing, 18, 2419
- Bengio, Y. 2009, Foundations and Trends® in Machine Learning, 2, 1, <http://dx.doi.org/10.1561/2200000006>
- Chandler, D. M., & Hemami, S. S. 2007, IEEE Transactions on Image Processing, 16, 2284
- Cornwell, T. J. 2008, IEEE Journal of Selected Topics in Signal Processing, 2, 793
- Deng, H., Zhang, D., Wang, T., et al. 2015, Solar Physics, 290, 1479
- Elad, M., & Aharon, M. 2006, IEEE Transactions on Image processing, 15, 3736
- Goodfellow, I., Pouget-Abadie, J., Mirza, M., et al. 2014, in Proceedings of the 27th International Conference on Neural Information Processing Systems, 2, 2672
- Hinton, G. E., Osindero, S., & Teh, Y.-W. 2006, Neural Computation, 18, 1527, <https://doi.org/10.1162/neco.2006.18.7.1527>
- Hinton, G. E., & Salakhutdinov, R. R. 2006, Science, 313, 504
- Högbom, J. 1974, Astronomy and Astrophysics Supplement Series, 15, 417
- Isola, P., Zhu, J.-Y., Zhou, T., & Efros, A. A. 2016, arXiv:1611.07004
- Johnson, J., Alahi, A., & Fei-Fei, L. 2016, ECCV 2016, Part II, Lecture Notes in Computer Science 9906, 694, https://link.springer.com/content/pdf/10.1007%2F978-3-319-46475-6_43.pdf
- Kupyn, O., Budzan, V., Mykhailych, M., Mishkin, D., & Matas, J. 2017, arXiv:1711.07064
- KupynOrest. 2019, GitHub Repository, <https://github.com/KupynOrest/DeblurGAN.git>
- LeCun, Y., Boser, B., Denker, J. S., et al. 1990, Neural computation, 1, 541, <https://doi.org/10.1162/neco.1989.1.4.541>
- LeCun, Y., Bottou, L., Bengio, Y., Haffner, P., et al. 1998, Proceedings of the IEEE, 86, 2278, <https://doi.org/10.1109/5.726791>
- Ma, S., Yin, W., Zhang, Y., & Chakraborty, A. 2008, in IEEE Conference on Computer Vision and Pattern Recognition, IEEE, 1
- Nah, S., Kim, T. H., & Lee, K. M. 2016, arXiv:1612.02177
- Rubinstein, R., Peleg, T., & Elad, M. 2012, IEEE Transactions on Signal Processing, 61, 661
- Rubinstein, R., Zibulevsky, M., & Elad, M. 2009, IEEE Transactions on Signal Processing, 58, 1553
- Rudin, L. I., Osher, S., & Fatemi, E. 1992, Physica D: Nonlinear Phenomena, 60, 259
- Simonyan, K., & Zisserman, A. 2014, Computer Science, arXiv: 1409.1556
- Su, M., & Basu, M. 2002, Pattern Recognition, 35, 2881
- Tian, C., Fei, L., Zheng, W., et al. 2019, Deep Learning on Image Denoising: An overview, arXiv:1912.13171
- Wakker, B. P., & Schwarz, U. 1988, A&A, 200, 312
- Wang, Z., Bovik, A. C., Sheikh, H. R., Simoncelli, E. P., et al. 2004, IEEE Transactions on Image Processing, 13, 600
- Wen, Y.-W., Chan, R. H., & Yip, A. M. 2011, IEEE Transactions on Image Processing, 21, 106
- Wenger, S., Magnor, M., Pihlström, Y., Bhatnagar, S., & Rau, U. 2010, PASP, 122, 1367
- Xiang, S., Meng, G., Wang, Y., Pan, C., & Zhang, C. 2015, International Journal of Computer Vision, 114, 248, <https://doi.org/10.1007/s11263-014-0755-z>
- Xu, L., Ren, J. S., Liu, C., & Jia, J. 2014, in Advances in Neural Information Processing Systems, 1, 1790, <https://dl.acm.org/doi/10.5555/2968826.2969026>
- Xu, L., Yan, Y., Ma, L., & Zhang, Y. 2018a, Multimedia Tools and Applications, 77, 20937
- Xu, L., Yan, Y., & Sun, W. 2018b, in American Geophysical Union, Fall Meeting Abstracts, 2018, SM31D-3528
- Yan, Q., & Wang, W. 2017, Adv. Neural Inf. Process. Syst., 8, 487
- Zhang, J., Zhao, D., & Gao, W. 2014, IEEE Transactions on Image Processing, 23, 3336
- Zhang, L., Zhang, L., Mou, X., & Zhang, D. 2011, IEEE Transactions on Image Processing, 20, 2378